

Ultrasonic Imaging

<http://uix.sagepub.com/>

Automatic Needle Detection and Tracking in 3D Ultrasound Using an ROI-Based RANSAC and Kalman Method

Yue Zhao, Christian Cachard and Hervé Liebgott

Ultrason Imaging 2013 35: 283

DOI: 10.1177/0161734613502004

The online version of this article can be found at:

<http://uix.sagepub.com/content/35/4/283>

Published by:



<http://www.sagepublications.com>

On behalf of:



Ultrasonic Imaging and Tissue Characterization Symposium

Additional services and information for *Ultrasonic Imaging* can be found at:

Email Alerts: <http://uix.sagepub.com/cgi/alerts>

Subscriptions: <http://uix.sagepub.com/subscriptions>

Reprints: <http://www.sagepub.com/journalsReprints.nav>

Permissions: <http://www.sagepub.com/journalsPermissions.nav>

Citations: <http://uix.sagepub.com/content/35/4/283.refs.html>

>> [Version of Record](#) - Sep 30, 2013

[What is This?](#)

Automatic Needle Detection and Tracking in 3D Ultrasound Using an ROI-Based RANSAC and Kalman Method

Ultrasonic Imaging

35(4) 283–306

© The Author(s) 2013

Reprints and permissions:

sagepub.com/journalsPermissions.nav

DOI: 10.1177/0161734613502004

ultrasonicimaging.sagepub.com



Yue Zhao¹, Christian Cachard¹, and Hervé Liebgott¹

Abstract

This article proposes a robust technique for needle detection and tracking using three-dimensional ultrasound (3D US). It is difficult for radiologists to detect and follow the position of micro tools, such as biopsy needles, that are inserted in human tissues under 3D US guidance. To overcome this difficulty, we propose a method that automatically reduces the processed volume to a limited region of interest (ROI), increasing at the same time the calculation speed and the robustness of the proposed technique. First, a line filter method that enhances the contrast of the needle against the background is used to facilitate the initialization of ROI using the tubularness information of the complete US volume. Then, the random sample consensus (RANSAC) and Kalman filter (RK) algorithm is used in the ROI to detect and track the precise position of the needle. A series of numerical inhomogeneous phantoms with a needle simulated from real 3D US volumes are used to evaluate our method. The results show that the proposed method is much more robust than the RANSAC algorithm when detecting the needle, regardless of whether or not the insertion axis corresponds to an acquisition plane in the 3D US volume. The possibility of failure is also discussed in this article.

Keywords

RANSAC algorithm, Kalman filter, line filter, motion estimation, 3D ultrasound

Introduction

Minimally invasive techniques are more and more widely used in medical examinations and surgeries. In many situations, radiologists use an ultrasound (US) scanner to view a micro tool such as a metal needle during its insertion to get tissue samples in the case of biopsy or to deliver the treatment dose in the case of radiation therapy. Several research groups have improved robotic-guided needle-insertion systems for real-time clinical application¹⁻³: Krupa et al.¹ have developed a robotic vision system that automatically detects and finds the positions of surgical tools during robotized laparoscopic surgeries; Bax et al.² have improved a robot

¹Creatis, Université de Lyon, CREATIS, CNRS UMR5220, Inserm U1044, INSA-Lyon, Université Lyon I, France

Corresponding Author:

Yue Zhao, Creatis, Université de Lyon, CREATIS, CNRS UMR5220, Inserm U1044, INSA-Lyon, Université Lyon I, France.

Email: yue.zhao@creatis.insa-lyon.fr

assisted 3D US-guided prostate biopsy system, which can help the physicians perform a double biopsy in the same target region; and Hong et al.³ have developed a needle-insertion robot for US-guided percutaneous cholecystostomy, which is able to compensate for the movement and deformation of the organ and correct the needle path. However, because of the limitations of the current robotic systems, most needle-insertion tasks are finished by the radiologists themselves. There are mainly two approaches for needle insertion: guided or freehand.⁴ In the guided needle approach, a system with a slot or hole attached to the probe is used, which serves to guide the needle along a desired route through the tissue. By contrast, the freehand approach is technically more challenging and takes longer to learn but it provides greater flexibility. In this approach, one operates the transducer with one hand while the other hand holds the needle unattached to the transducer. To date, the guided approach has been carried out using mainly a two-dimensional (2D) US probe. During the procedure, it is necessary to tilt and rotate the probe so as to align the US beam and the needle tip.⁵ Some useful assistant devices have been developed to help in the alignment, for example, the LOGIQ E9 system from GE Healthcare (Little Chalfont, Buckinghamshire, United Kingdom). It provides a needle assembly that consists of a sheath and stylet, which houses a removable and reusable electromagnetic sensor. There is also a navigation system that can predict the path of the needle tip on the US scanner, as the iU22 xMATRIX US system with PercuNav (Philips Healthcare, Koninklijke Philips N.V., Amsterdam, The Netherlands), which uses an electromagnetic navigation technology to locate the tip of the needle or other instruments in real time, and also guides the instruments to the target region. However, this type of device increases the cost of the procedure. Moreover, metal needles and tissues are three-dimensional (3D) structures, and most of the time the needle does not correspond well to the 2D US plane. Only a part of the needle is visible. Other times, the radiologist can see the tissues and organs clearly, but the needle cannot be found. This increases the risk of injuring normal tissues. As a result, interest in 3D US guidance and computer-aided localization technologies has been increasing.

As needle identification using 2D or 3D US remains one of the hottest research topics in the domain of medical US, several emerging technologies have been recently developed. Fronheiser et al.⁶ use 3D color Doppler to track a vibrating needle at kilohertz frequencies. Nichols et al.⁷ test the visibility of needles with different echo enhancement modifications in the change in angles of insonification, which can be applied in 2D or 3D US. Rotemberg et al.⁸ develop a three-step segmentation algorithm that can identify a needle in an acoustic radiation force impulse (ARFI) image and overlay the needle prediction on a 2D co-registered B-mode image. The above-mentioned needle identification methods use a complementary technology, like vibration or hyperechoic coating, to help to detect the needle position using US imaging. The methods below only use the intensity information and computed assisted algorithm to locate the needle using 2D or 3D US scanners. Draper et al.⁹ use a threshold to segment the 2D variance image that is calculated from the original 2D US image, and then perform principal components analysis (PCA) on the binary image after the threshold to find the direction of the needle. Finally, the tip can be found by masking the line direction with the binary image. However, the authors do not apply their method to the 3D US volume. Wei et al.^{10,11} use a threshold method to detect and track prostate brachytherapy needles. The differences between voxels are obtained by subtracting a live-scan 3D US volume and a prescan US volume performed before insertion of the needle. Then, by threshold, the background noise is removed and the voxels of the needle are detected. Finally, the 3D US volume is reconstructed. With robotic assistance, their method can achieve high accuracy, but the registration of the prescan and postscan volume remains a problem and the use of a robot strongly limits the field of application and increases the system's cost dramatically. Hough transform (HT)-based algorithms are also used as needle localization approaches.¹²⁻¹⁴ Hartmann et al.¹² use the 3D HT method to segment the needle on the prostate

biopsy images; Zhou et al.¹³ propose an improved 3D HT by adding a coarse-fine search strategy to automatically segment the needle in 3D US volumes; and Qiu et al.¹⁴ use 3D quick randomized HT (3DQRHT) to segment the needle in a water phantom. However, these authors do not report results based on an inhomogeneous background 3D US volume, neither in a dynamic tracking situation. Barva et al.¹⁵ use the parallel integral projection (PIP) transform to extract the axis of the needle. They considered the maximum PIP transformation as the axis of the needle, and the hierarchical mesh-grid search was implemented to determine the axis position. The weakness of this method is its long calculation time that cannot match the requirements of real-time applications. The random sample consensus (RANSAC) method¹⁶ is also applied for biopsy needle localization in 3D US volumes^{17,18} as well as other methods such as line filtering¹⁹ and phase grouping.²⁰

The RANSAC algorithm has been proposed for biopsy needle localization in 3D US volumes.^{17,18} Unlike the projection-based methods, this method is proven to be faster and more robust in localizing high-intensity structures. Uherčík and colleagues¹⁷ tested the model-fitting RANSAC algorithm with simulated data created using the software package Field II^{21,22} as well as high-quality real-time US data. Using the model-fitting RANSAC algorithm, an accuracy of less than 1 mm was reported for the axis and tip positions compared with the ground truth value. However, in real situations, the 3D US volumes are not of such high quality. In particular, they often have a complicated inhomogeneous background with structures that might appear as needles in the US data. The presence of these structures leads to a decreased robustness and increased processing time for the model-fitting RANSAC method.

The RANSAC algorithm is an iterative method used to estimate the parameters of a preset mathematical model from a data set that contains inlier points, which can be approximately fitted to a model, and outlier points, which cannot be fitted to this model. In image processing, it is used to detect line-like or circle-like features. Unlike conventional sampling techniques that use as much of the data as possible to obtain an initial solution, RANSAC uses the smallest set possible to form the model and then proceeds to enlarge this set with consistent data.¹⁶ For a line structure, the RANSAC procedure chooses only two points from the whole data set to form one linear model in one iteration, and then calculates the model cost involving all the points. After all the iterations, the cost of different models is compared, and the minimum cost model is considered as the best-fitting model for the data set. However, speckle noise is always present in a 3D US volume, with the voxels of highest intensity typically located at the depths closest to the transducer. Even worse, some linear structures of the tissue can also display a line form very similar to the needle in 3D US volumes. All these reasons increase the risk of a bad model fitting from the RANSAC algorithm. The usual solution is to raise the number of iterations to increase the successful percentage of a best model; notwithstanding, the large iteration number also increases the processing time and may lead to false model estimation. In this situation, the model-fitting RANSAC algorithm loses its robustness and time-saving advantage.

To enhance the robustness of the RANSAC algorithm, and simultaneously reduce the running time, we propose a strategy for automatically choosing a region of interest (ROI) in combination with the RANSAC and Kalman filter (ROI-RK) algorithm. While the principle of an RK method is presented in Zhao et al.,²³ the contribution of the present study is substantial. Indeed, in Zhao et al.,²³ the algorithm can only run in a homogeneous background. Moreover, because the whole 3D US volumes are used in Zhao et al.,²³ the calculation time is quite long. We propose here the introduction of an ROI strategy and evaluate in more detail the precision and robustness of the proposed technique.

This article is organized as follows: the second section presents the indications of the methods used, the third section explains the simulation, and the fourth section gives the simulation results. The discussion and conclusion are given in the last two sections.

Method

Global View of ROI-RK Method

It is very difficult for radiologists to detect the correct US plane that contains the needle in the 3D US volume. Therefore, automatic needle detection methods for 3D US volumes have become very important. There are several challenges for the existing model-fitting RANSAC algorithm. First, the 3D US volume has speckle noise, and certain parts of tissue may have the same level of intensity as the needle; in this situation, the RANSAC algorithm can fail. Second, there are tens of thousands of voxels in a 3D US volume, which can lead to a large number of calculations. Third, this method can detect the needle in only one single 3D US volume. For the tracking task, it is not robust enough to follow the position of the needle in a series of real-time acquisition of 3D US volumes. The ROI-RK method proposed in this article aims at overcoming these limitations. It consists of two steps that are given in Figure 1.

Step 1: Initializing step—A 3D line filter²⁴ (Appendix A) is used in the complete 3D US volume to obtain a tubularness image. The RANSAC algorithm runs in this image to get the initial position of the needle, and it initializes the ROI.

Step 2: Tracking step—Only inside the ROI is the biopsy needle detected and tracked in three steps: (1) the RANSAC algorithm is used to detect the position of the needle in the ROI; (2) speckle tracking is used to estimate the velocity of the needle tip; and (3) the Kalman filter is used to update the ROI and refine the position of the needle.

Step 1: Initializing ROI

In the original 3D US volume, there are needle voxels and inhomogeneous background voxels. The line-like structures from the inhomogeneous background become outliers and influence the result of RANSAC. Without restricting the processed data to a limited ROI that contains the needle, the use of RANSAC in the whole US volume confuses the background tissue and needle, and thus yields a false needle position. Unfortunately, for the initial volume, even a rough position of the needle is not known. As a result, the complete volume must be processed so as to initialize the ROI used in the remaining part of the algorithm. To reduce the risk of false detection, a 3D line filter initially proposed by Frangi et al.²⁴ and previously used by our group¹⁹ is applied to enhance the contrast between the needle and the background. The line filter is an efficient way to reduce false detection, but it is expensive from a calculation point of view. We thus use it only for the initialization of the ROI.

Let $V(M(x, y, z), I(M))$ be the set of voxels of a 3D US volume having two characteristics for each voxel: $M(x, y, z)$ and $I(M)$ represent the position and intensity of the voxels, respectively. According to the shape of the biopsy needle, the ROI can be defined as a cylinder of radius R_{ROI} . Suppose that $l(t; \mathbf{A})$ and V_{roi} are the axis of the cylinder and the subset of the voxels within the ROI, respectively. The axis is defined by a parametric equation where \mathbf{A} is a coefficient matrix and t is the parameter (Appendix B). Then the V_{roi} satisfies the following condition:

$$V_{\text{roi}} = \{M \in V \mid d(M, l(t; \mathbf{A})) \leq R_{\text{ROI}}\}, \quad (1)$$

where $d(M, l(t; \mathbf{A}))$ is the Euclidean distance from the point M to the line $l(t; \mathbf{A})$. To obtain the axis $l(t; \mathbf{A})$, the line filter is used in the whole 3D US volume to reduce the speckle noise and enhance the contrast between the needle and the background. With this method, the original US volume can be turned into a 3D tubularness volume (Appendix A). The model-fitting RANSAC

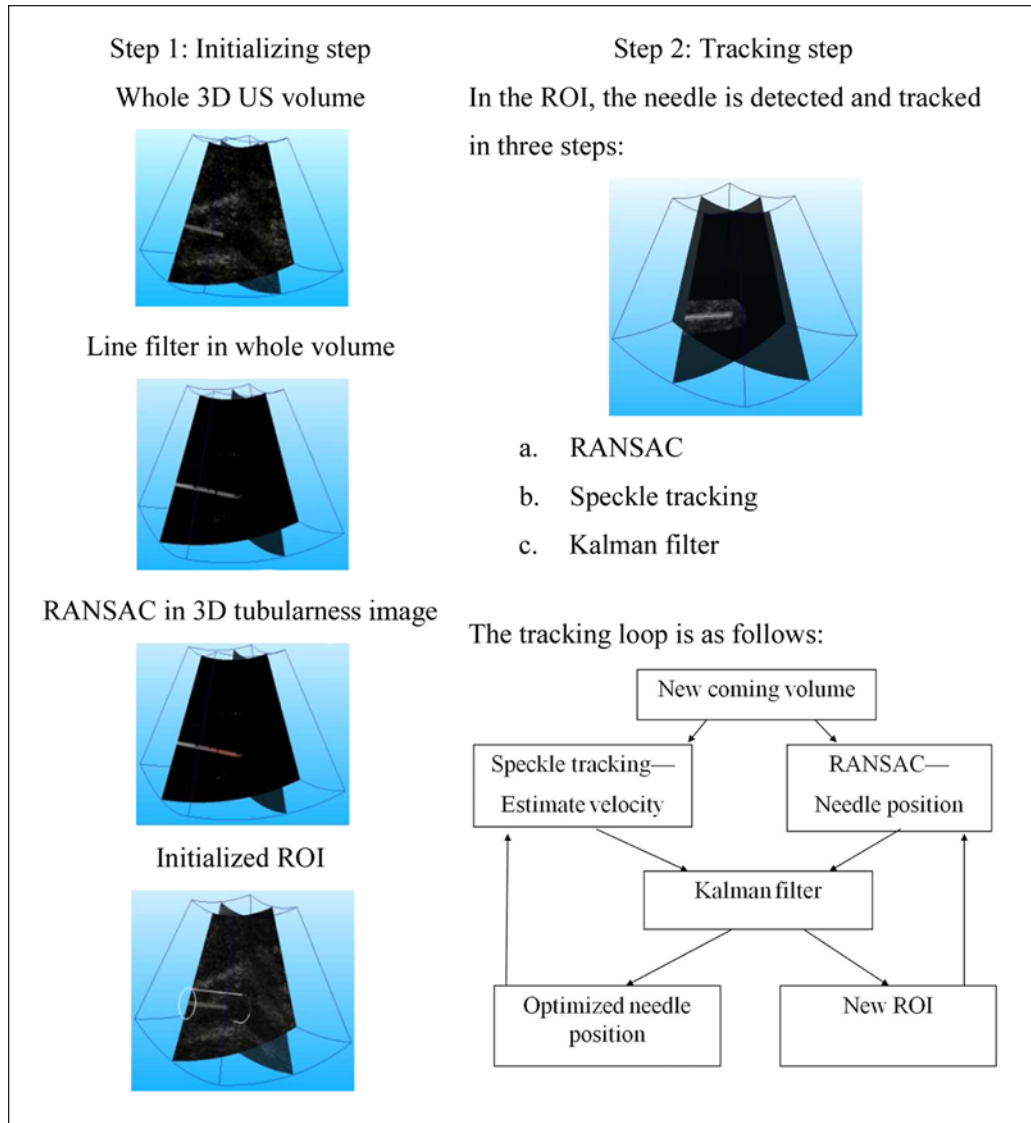


Figure 1. A global view of the ROI-RK method.

Note. ROI-RK = ROI in combination with the RANSAC and Kalman filter; 3D US = three-dimensional ultrasound; ROI = region of interest; RANSAC = random sample consensus.

algorithm (presented in the “Model-Fitting RANSAC Algorithm” section) runs throughout this tubulerness volume and obtains the points for constructing the coefficient matrix A . Once this matrix A is fixed, the axis of the ROI can be also fixed, and the ROI is deduced from this result. After the initialization, the line filter is no longer used.

Step 2: Tracking Procedure

Once the ROI has been initialized, the proposed method processes only the voxels inside the ROI. As presented in the introduction of this section, the tracking consists of three steps:

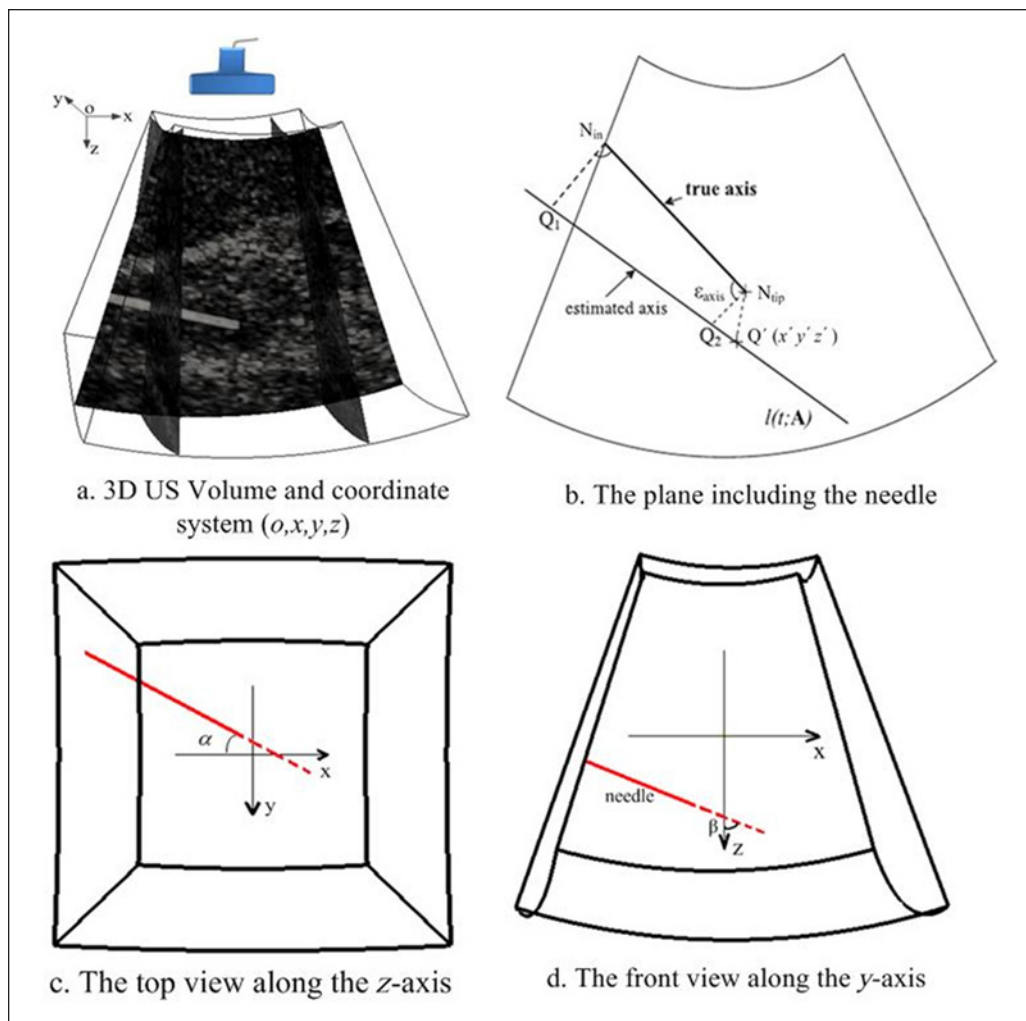


Figure 2. 3D US volume and definitions of geometric parameters.

Note. 3D US = three-dimensional ultrasound.

RANSAC, speckle tracking, and Kalman. The organization of the different steps is governed by the mathematical model chosen for the Kalman filter, which is first described herein.

Mathematical model for Kalman filter. The objective of the proposed method is to detect and track the position of a biopsy needle using the Kalman filter (Appendix C). To fix a line in the 3D space, three parameters are needed. These parameters are chosen as direction angles α (the angle between the needle and the plane xoz), β (the angle between the needle and the positive direction of z -axis) and the tip position (needle end point, Figure 2c and 2d). As the insertion of the needle and the 3D US probe are controlled manually, the inserting speed of the needle can change from time to time. Moreover, the needle in the US volume is not only moving along the axis direction but a rotation and even motion along the z -axis can also occur. As a result, the speed of variation of the two angles α , β and the needle tip should be included in the measurement vector.

This leads to the state vector $\mathbf{S} = [\beta, \alpha, v_\beta, v_\alpha, \mathbf{p}_t, \mathbf{v}_t]^T$ and the following time update equation:

$$\hat{\mathbf{S}}_k^- = \mathbf{F} \hat{\mathbf{S}}_{k-1}, \quad (2)$$

$$\mathbf{P}_k^- = \mathbf{F} \mathbf{P}_{k-1} \mathbf{F}^T + \mathbf{Q}, \quad (3)$$

where $\mathbf{F} = \begin{bmatrix} \mathbf{I}_{2 \times 2} & \mathbf{0}_{2 \times 6} & \mathbf{0}_{2 \times 6} \\ \mathbf{0}_{2 \times 2} & \mathbf{I}_{2 \times 2} & \mathbf{0}_{2 \times 6} \\ \mathbf{0}_{3 \times 4} & \mathbf{0}_{3 \times 3} & \mathbf{I}_{3 \times 3} \end{bmatrix}$, $\mathbf{p}_t = [x_t, y_t, z_t]$ is the coordinate of N_{tip} , and

$\mathbf{v}_t = [v_{tx}, v_{ty}, v_{tz}]$ is the velocity vector of the needle tip. The processing noise is assumed as Gaussian, which is the classic processing noise used in Kalman filters.²⁵ The measurement vector \mathbf{Z} is set as $\mathbf{Z} = [\beta, \alpha, \mathbf{p}_t, \mathbf{v}_t]^T$ because the two angles and the tip position can be measured by the RANSAC algorithm (“Model-fitting RANSAC algorithm” section), and the velocity can be estimated by the movement estimation method (“Motion estimation” section). According to Equation (C2; Appendix C), the measurement matrix is $\mathbf{H} = \begin{bmatrix} \mathbf{I}_{2 \times 2} & \mathbf{0}_{2 \times 8} \\ \mathbf{0}_{6 \times 4} & \mathbf{I}_{6 \times 6} \end{bmatrix}$. The measurement noise is also a Gaussian distribution that is estimated by a large number of repeat trials. In the case of a robotic-driven needle insertion, there will be a control vector \mathbf{u} and control matrix \mathbf{B} as input. In our application, the needle is actuated by hand. The control input is unknown, thus the \mathbf{B} and \mathbf{u} in Equation (C1; Appendix C) are set to zero.

Tracking loop. Once the ROI is initialized, the tracking loop can begin. The RANSAC algorithm (described in section “Model-Fitting RANSAC Algorithm”) runs in this ROI to obtain the needle axis and tip position \mathbf{P}_t . As the needle axis $l(t; \mathbf{A})$ is estimated using the RANSAC algorithm, the unit vector of the axis $\mathbf{u} = [u_x, u_y, u_z]$ is easy to get, and the two angles α, β are calculated:

$$\alpha = \arctan\left(\frac{u_y}{u_x}\right), \quad \beta = \arccos\left(\frac{u_z}{\|\mathbf{u}\|}\right). \quad (4)$$

When the second volume comes, the inserting velocity \mathbf{v}_t is obtained using the speckle tracking method (section “Motion Estimation”). The initial velocities v_α, v_β are set to zero. Now there is enough information to initialize the Kalman filter. As the needle and the probe have a relative motion, and the ROI is quite limited, the ROI of the first volume may not be suitable for the next volume; therefore, the ROI in the new incoming US volume should be updated using the previous information. The time update equation of the Kalman filter is used to predict the new position of the needle in the new incoming US volume. Equation (5) calculates the state vector $\hat{\mathbf{S}}_k^-$ based on the state vector $\hat{\mathbf{S}}_{k-1}^-$ of the $k-1$ step. From $\hat{\mathbf{S}}_k^-$, the predicted needle tip $\hat{\mathbf{P}}_{tk}^-$, and the angles $\hat{\alpha}_k^-$ and $\hat{\beta}_k^-$ can be obtained, so the predicted ROI can be defined. Then the RANSAC algorithm is applied in the updated ROI to get the measurement vector for the Kalman filter. After that, the measurement update equations of the Kalman filter (Equations (C5)-(C7) in Appendix C) are used to optimally estimate the position of the needle, the posteriori state vector $\hat{\mathbf{S}}_k$ can be calculated, and more precise position information of the needle is obtained. All of this is a single loop in our method, and this loop continues until the end of the tracking procedure.

Model-fitting RANSAC algorithm. A model-fitting approach proposed by Uherčík¹⁷ uses the RANSAC algorithm and is applied to detect the two angles α, β and the tip position \mathbf{P}_t of a needle in the 3D US volume. The method is based on the following two assumptions:

1. The intensity of the needle voxels is higher than the tissue background.
2. The needle is a thin, long, and straight cylinder. Here, the biopsy needle or therapeutic probe used has a diameter of around 1 mm, thus it remains straight during insertion.

The proposed RANSAC algorithm consists of four steps:

Step 1: Classifying by threshold—this step aims to reduce the number of voxels based on the Assumption (1). In a 3D US volume, the needle voxels represent less than 1% of the whole volume. Consequently, the smallest threshold is set when the value is larger than 99% of the intensities of the background.

Step 2: Axis localization—this step uses the RANSAC algorithm to estimate an approximate position of the needle axis. Here the shape of the needle follows from the Assumption (2). This step returns the roughly estimated needle position defined by two points.

Step 3: Local optimization—this step uses a local optimization algorithm to find a more accurate position of the needle using the result of RANSAC.

Step 4: Tip localization—this step uses the sharp change of intensity along the axis of the needle estimated in Step 3 to identify its endpoint.

The output of the algorithm consists of $l(t; \mathbf{A})$, the axis equation from which the angles α, β are easily calculated and the tip position \mathbf{P}_t that is directly calculated in Step 4 of the RANSAC procedure.

Motion estimation. In medical US, there are different state-of-the-art algorithms for motion estimation, for example, block-matching and optical flow. The speckle tracking method, which belongs to the branch of block-matching algorithms, is selected here because it can directly track the back-scattered echoes generated by ultrasonic scatterers in tissue.²⁶ This method was first described by Robinson et al.,²⁷ and then applied by Trahey et al.²⁸ It was first used to detect the blood velocity with US data. It estimates velocities based on the displacement of a speckle pattern in the axial, lateral, and elevation directions. In our applications, the expected motion of the speckle pattern of the background tissue is stationary, except that when the needle is inserted, it is sheared apart. The motion of the speckle pattern of the needle is a translation motion along the axis direction, and there is no deformation along the insertion direction because the needle is thick enough. However, considering that there could be a slight relative motion between the needle and the probe, as pressing and rotating, there can be a movement of the axis within the ROI in the 3D volume. Here, the speckle tracking method is used to measure the speed of the needle tip \mathbf{v}_t . First, a small 3D region is chosen in the first volume as the kernel region, which is selected according to the coordinates of the estimated tip position. Then, a larger region is chosen as a searching region in the second volume. During the tracking procedure, the kernel region slides voxel by voxel in the searching region, and the normalized cross-correlation (NCC) is used to compare the similarity between the kernel region and the searching region. The 3D NCC is given as

$$\rho(a, b, c) = \frac{\sum_{i=1}^m \sum_{j=1}^n \sum_{k=1}^p [\mathbf{X}_0(i, j, k) - \bar{\mathbf{X}}_0] [\mathbf{X}_1(i + a, j + b, k + c) - \bar{\mathbf{X}}_1]}{\sqrt{\sum_{i=1}^m \sum_{j=1}^n \sum_{k=1}^p [\mathbf{X}_0(i, j, k) - \bar{\mathbf{X}}_0]^2 \sum_{i=1}^m \sum_{j=1}^n \sum_{k=1}^p [\mathbf{X}_1(i + a, j + b, k + c) - \bar{\mathbf{X}}_1]^2}}, \quad (5)$$

with ρ the correlation coefficient; \mathbf{X}_0 the kernel region, whose size is $m \times n \times p$; and \mathbf{X}_1 the searching region. The size of ρ is related to the sizes of \mathbf{X}_0 and \mathbf{X}_1 . Suppose that \mathbf{X}_1 is of size $M \times N \times P$, the size of ρ is $(M - m + 1) \times (N - n + 1) \times (P - p + 1)$. However, the traditional NCC does

not match all the requirements of real-time applications; for this point, the fast normalized cross-correlation (FNCC) algorithm²⁹ is chosen to overcome this difficulty. To calculate the numerator of Equation (5), the fast Fourier transform (FFT) is used to transfer the numerator part to the 3D frequency domain. After the multiplication, the inverse FFT (IFFT) is applied to turn back the result to the spatial domain. The denominator part is calculated using the summed-area tables algorithm,³⁰ which effectively reduces the processing time. With the FNCC algorithm, the computational efficiency is improved compared with the NCC algorithm. The best matching region is $\rho = \rho_{\max}$. The difference of coordinate between the kernel region and the best matching region indicates the displacement of the needle, thus the speed of the needle is obtained by dividing the displacement by time. It is used as an input measurement of the Kalman filter mentioned in the section “Mathematical Model for Kalman Filter.”

Simulation

To validate the advantages of our proposed ROI-RK method, a series of 3D US volumes are simulated. The inhomogeneous US background is simulated using Field II.^{21,22} The spatial arrangement of the background scatterers is chosen as a random uniform distribution. The density is 10 scatterers/mm³. Then, we use the intensities of voxels from an experimental 3D US volume of breast tissue acquired with a GE Voluson E8 scanner using a 12 MHz probe to calculate a scattering map. Each scatterer is assigned the value from this map corresponding to its spatial coordinates. This results in an inhomogeneous US background. It contains complicated patterns such as line-like structures. Each 3D US volume contains 55 planes, 64 beams/plane, and 160 samples/beam. The sector angle ϕ of one US volume is 34.5°, and the total tilt angle θ of the scan plan is 38°. The sample frequency for the envelope is 2.5 MHz. The axial resolution is about 0.3 mm, the lateral resolution is about 0.7 mm, and the azimuthal resolution is about 0.9 mm.

The needle voxels are added in the US volume to have a known ground truth position. Their intensity follows a distribution evaluated on experimental data as follows. A $50 \times 50 \times 50$ mm³ polyvinyl alcohol (PVA) cryogel phantom,³¹ containing 10% of PVA and 1% of silicate powder, was constructed and scanned with a Sonix MDP scanner equipped with a 4DC7-3/40 3D probe, after a thin metal needle of 0.6 mm radius was inserted. The needle was manually segmented 10 times by an expert. The corresponding amplitude distribution was estimated from eight scanned series of 3D US volumes. All the voxels of the needle were saved to generate the histogram of intensities and fitted with Gaussian distribution as represented in Figure 3.

From Figure 3, the parameters of the Gaussian distribution of the needle voxels are measured to be $\mu = 140$ and $\sigma = 28$.

$$f(x|\mu, \sigma) = \frac{1}{\sigma\sqrt{2\pi}} e^{-\frac{(x-\mu)^2}{2\sigma^2}}. \quad (6)$$

Two groups of simulated 3D US volumes have been generated. The first group is used to test the robustness of ROI-RK method compared with RANSAC only method with different insertion angles, and a constant contrast ratio (CR). The second group is used to test the performance of ROI-RK method with different CR values. For testing the method, if a Euclidean distance larger than 3 mm exists between the estimated tip and the real tip position, or between the estimated axis and the real axis, the method is considered to fail. The useful simulation parameters are shown in Table 1. For different insertion angles, the angle α is changed from the position corresponding to the scan plane to the position perpendicular to the scan plane. The angle β remains the same because the extreme positions, for example, the needle is parallel or almost parallel to the US propagating direction, are inconvenient for the radiologist to operate. The value of β is

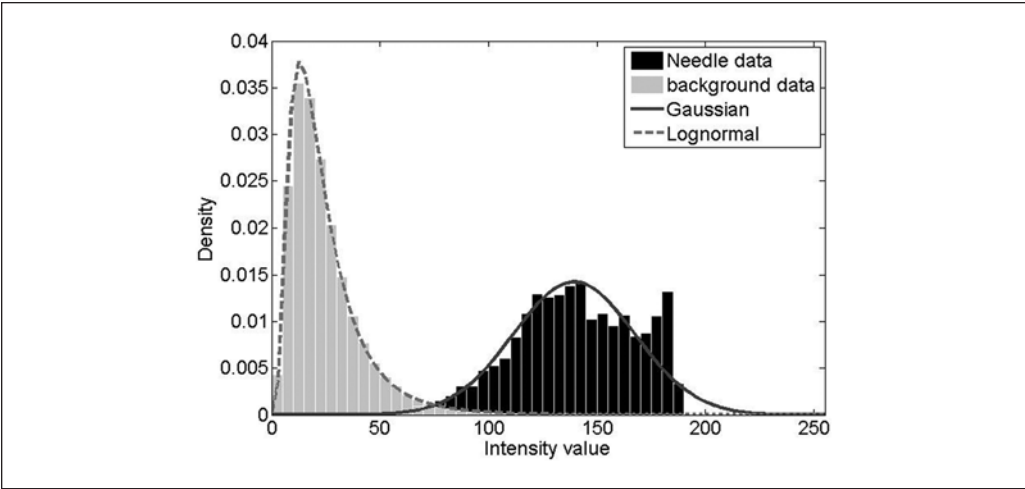


Figure 3. Distribution of the background voxels and the needle voxels of the phantom used on simulation.
Note. The background voxels are fitted with a lognormal distribution, and the needle voxels are fitted with a Gaussian distribution.

Table 1. The Useful Simulation Parameters for the Needle.

Parameters	Group 1: The Influence of the Insertion Angle with Constant CR	Group 2: The Influence of the Varied CR with the Same Inserting Angle
Needle length (mm)	6-25	6-25
Needle radius (mm)	0.5	0.5
α (degree)	0°, 30°, 60°, 90°	0°
β (degree)	73°	73°
CR	4.7	2.0-3.5

Note. CR = contrast ratio.

selected as a practice direction. What should be also mentioned is that the range of CR (2.0-3.5) is set according to the real 3D US volumes.

Results

The proposed ROI-RK method results were evaluated quantitatively and compared with the previously obtained results of the RANSAC algorithm used alone.¹⁷ Mean error and standard deviation (STD) of error were calculated. Each simulation was repeated 20 times.

$$\bar{\mathbf{e}} = E[\hat{\mathbf{x}}_i - \mathbf{x}_r]. \tag{7}$$

$$\text{STD} = \left(\frac{1}{n-1} \sum_{i=1}^n (\hat{\mathbf{e}}_i - \bar{\mathbf{e}})^2 \right)^{\frac{1}{2}} \tag{8}$$

where $\hat{\mathbf{x}}_i$ is the i th estimated result, \mathbf{x}_r is the ground truth value, $\hat{\mathbf{e}}_i$ is the i th measurement error, $\bar{\mathbf{e}}$ is the mean error, and n is the number of repetitions. The axis accuracy $\varepsilon_{\text{axis}}$ and the tip error $\|N_{\text{tip}}Q\|$ are illustrated in Figure 2b: N_{in} is the real insert position, N_{tip} is the real tip, and $l(t; \mathbf{A})$ is the estimated axis. Q_1 and Q_2 are the orthogonal projections of N_{in} and N_{tip} on the estimated axis, respectively. $Q'(x', y', z')$ is the estimated tip position. The tip accuracy is defined as the error between the x, y, z and x', y', z' separately. $\varepsilon_{\text{axis}}$ is defined as the maximum of the Euclidean distance of $\|N_{\text{in}}Q_1\|$ and $\|N_{\text{tip}}Q_2\|$.

Influence of Insertion Angle at Fixed CR

In this first series of simulations, the needle is inserted in the background at the fixed velocity of 1 mm/s along its axis. Between the beginning and the end of the sequence, the needle insertion varies between 6 and 25 mm. Four different values of angles α ($0^\circ, 30^\circ, 60^\circ, 90^\circ$) (Figure 2c) of the position are simulated, whereas $\beta = 73^\circ$ (Figure 2d) in all the simulated volumes. The CR defined as

$$\text{CR} = \frac{\bar{I}(N_{\text{needle}})}{\bar{I}(N_{\text{ROI}})} \quad (9)$$

is maintained constant and equal to 4.7 for all the experiments presented in this section. The ROI is selected as a cylinder, whose axis is the axis of the needle, and whose radius is five times the radius of the needle. N_{needle} represents the voxels closer to the axis than the needle radius. The remaining voxels are considered as the background voxels. The results of the different metric errors for $\alpha = 30^\circ$ are represented in Figure 4.

From Figure 4, the mean error of the RANSAC algorithm is always significant, while that of the ROI-RK algorithm is very close to zero. This means that with the inhomogeneous background, the RANSAC cannot estimate the position of the needle well. The STD of the error of the ROI-RK is much smaller than that of the RANSAC algorithm, demonstrating that the ROI-RK method is more robust than the RANSAC algorithm to inhomogeneous background derived from breast scattering maps. Although sometimes the mean error of the RANSAC algorithm is equal or smaller than that of the ROI-RK method, this is only a fortuitous result, it cannot affect the average performance of the algorithm. What should be mentioned is that the change of insertion angle of the needle will slightly influence the performance of the ROI-RK method. For the tip localization, if the coordinate is closer to the axis direction, the STD of the error will be smaller. Table 2 shows the STD improvement of error of the ROI-RK algorithm compared with the RANSAC algorithm with the different α . The improvement percentage is calculated as

$$I_{\text{per}} = \left(1 - \frac{\overline{\text{STD}}_{\text{ROI-RK}}}{\overline{\text{STD}}_{\text{RANSAC}}} \right) \times 100. \quad (10)$$

The high percentage improvement proves that the ROI-RK algorithm has largely increased the robustness of the needle position detection with the inhomogeneous background imitating the US response of breast tissues.

The ROI-RK method is also less time-consuming than RANSAC. Equation (B8) in Appendix B gives the iteration number J of the RANSAC algorithm. This number is updated during processing according to the inlier ratio. The larger the inlier ratio, the smaller the iteration number, and the faster the needle position can be estimated. To limit the processing time in the simulation, the maximum iteration number is set to 50. As convergence is not attained when the RANSAC algorithm reaches the number of 50 iterations, the position of the needle does not fit for a proper model. This leads to a high STD error.

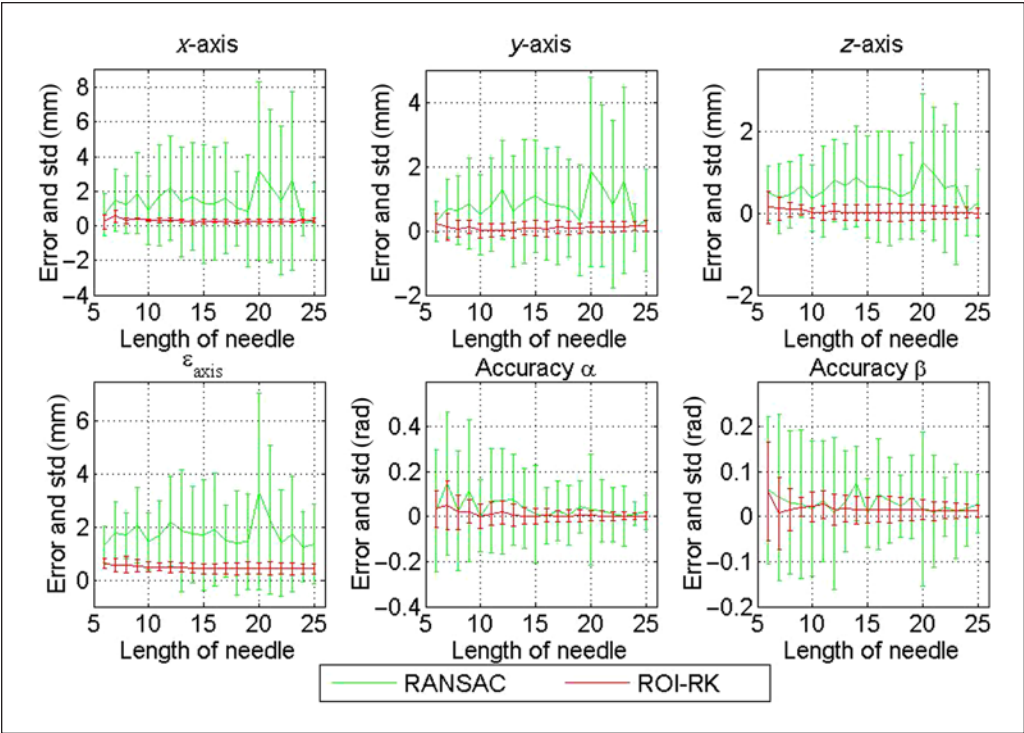


Figure 4. The mean and the STD of the tip error (the first line), $\varepsilon_{\text{axis}}$ (second line, left), α (second line, middle), and β (second line, right) for the RANSAC and ROI-RK detection methods with $\alpha = 30^\circ$ and $\beta = 73^\circ$.
Note. RANSAC = random sample consensus; ROI-RK = region of interest in combination with the RANSAC and Kalman filter.

Table 2. Improvement of the STD of the ROI-RK Method Compared with the RANSAC Method.

Improvement According to Different α						
α	x-Axis (%)	y-Axis (%)	z-Axis (%)	Axis Accuracy (%)	α (%)	β (%)
0°	90	13	70	60	72	67
30°	91	76	70	71	72	63
60°	85	88	86	84	68	80
90°	31	92	87	83	63	86

Note. ROI-RK = region of interest in combination with the RANSAC and Kalman filter; RANSAC = random sample consensus.

To get the same performance, RANSAC and ROI-RK were tested with the same 3D US volume. Because the RANSAC algorithm uses the whole volume, the maximum inlier ratio ζ_R is 0.05, while the inlier ratio of the ROI-RK method ζ_p stays above 0.4. Equation (B8) in Appendix B is used to estimate the iteration number of each method, thus J_R is about 1840 for RANSAC and J_p is about 26 for ROI-RK. This explains why convergence is not attained in our case, as the iteration number is set to 50. To attain similar performances, without limiting the number of iterations, RANSAC takes 10 times longer than the proposed method. In Uherčík

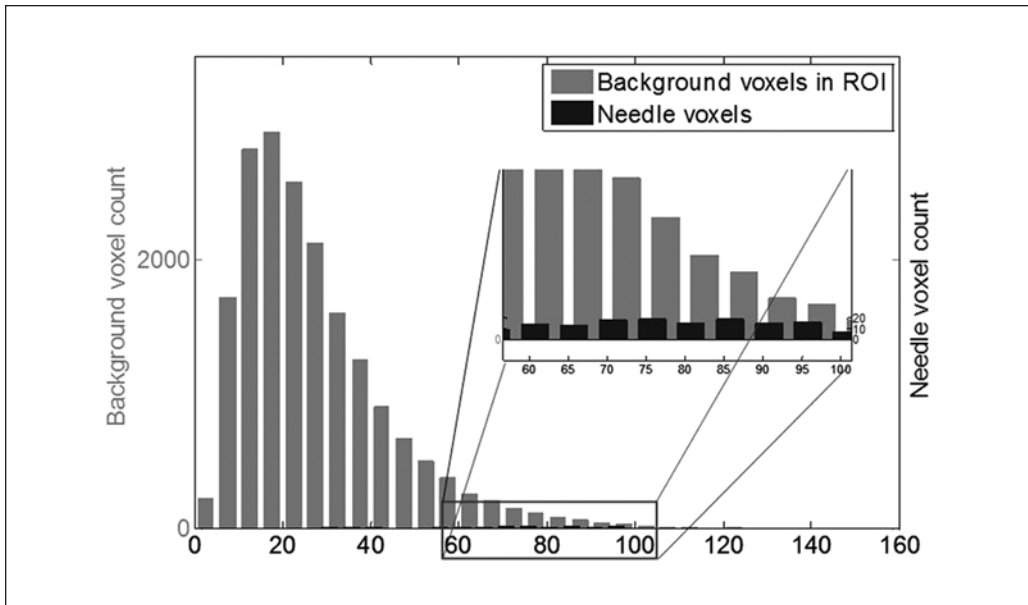


Figure 5. An example of the count of the background voxels and the needle voxels on the same scale. Note. The scale of the needle voxels can be seen in the enlarged view of the region in the square. ROI = region of interest.

et al.,¹⁷ a running time less than 1 s is claimed of RANSAC when locating the needle in a 3D US volume. As the ROI-RK method is less time-consuming, and for the existing US scanner, it takes about 1 s to generate a 3D US volume, the proposed method will satisfy the real-time clinical applications.

Influence of the CR

In this section, the influence of the CR on the failure conditions of ROI-RK is evaluated. All the other parameters, for example, the distance from the probe to the needle or the orientation of the needle, are fixed. The needle is still in a dynamic situation with an inserting velocity along the axis direction of 1 mm/s. The intensity of the digital image coded with 8 bits varies from 0 to 255. The range of the threshold is chosen between 60 and 100 stepped by 5. The simulation is performed to reach a CR between 2 and 3.5 (μ in Equation (6)) is from 70 to 115 stepped by 5). As the CR is calculated from the intensities, and because these intensities are chosen in regular steps, the CR values are not separated by a constant step. To visualize the distributions of the voxel intensities, in the needle and in the background, the different counts inside the ROI are given as histograms in Figure 5.

Table 3 presents the failure rate for the different CRs depending on different threshold values. If a Euclidean distance larger than 3 mm exists between the estimated tip and the real tip, or between the estimated axis and the real axis, the method is considered to fail. From each column in Table 3, one can observe that when the CR is fixed, the higher the threshold value is, the more times the ROI-RK method fails. Figure 6 shows the histogram of the distributions of the background voxels in the ROI and needle voxels. The threshold value changes from 60 to 85 while the CR is kept equal to 2.5. From Figure 6, it is clear that with the growth

Table 3. The Failure Rate of ROI-RK Method Depending on Different CR and Threshold.

Failure Rate (%)	CR in ROI									
	2.0	2.2	2.4	2.5	2.7	2.8	3.0	3.2	3.4	3.5
60	72%	32%	6%	4%	2%	6%	6%	0%	0%	4%
65	100%	44%	16%	4%	4%	8%	2%	4%	2%	2%
70	100%	78%	60%	48%	0%	0%	0%	0%	2%	0%
75	—	100%	100%	96%	0%	2%	0%	2%	0%	0%
80	—	—	100%	100%	24%	6%	0%	0%	0%	0%
85	—	—	—	100%	100%	70%	0%	0%	2%	0%
90	—	—	—	—	100%	86%	58%	0%	2%	0%
95	—	—	—	—	—	100%	100%	26%	4%	0%
100	—	—	—	—	—	—	100%	100%	88%	2%

Note. ROI-RK = ROI in combination with the RANSAC and Kalman filter; CR = contrast ratio; ROI = region of interest; RANSAC = random sample consensus.

of the threshold, although more and more background voxels are eliminated by threshold, some needle voxels are also excluded. Table 4 gives the average inliers count with the same CR = 2.5; the threshold value changes from 60 to 85. The inliers count is an average value because the needle length is different. Figure 7(a-f) shows the different appearances of the needle after the different thresholds in the 3D US volume when the CR = 2.5, corresponding to Figure 6(a-f). A large threshold value can limit the influence of the speckle noise of the background; moreover, it also deletes the needle voxels whose intensity is less than this threshold. Obviously, the incomplete structure of the needle leads to the failure of the ROI-RK method. From each line in Table 2, it is apparent that when the threshold value is fixed, the higher the CR is, the more robust the ROI-RK method is. Figure 8 shows the histogram of six different CRs (from 2.4 to 3.2) of the background voxels and the needle voxels. With the increase in the CR, more and more needle voxels pass the threshold and make the structure of the needle more distinct (Figure 9). With the complete structure of the needle, even though the speckle noise still exists, the ROI-RK method does not fail. From Figures 6 to 9, one can conclude that if the structure of the needle is relatively complete, regardless of whether the background is noisy or not, the ROI-RK method can detect and track the needle position well.

Discussion

The objective of this study is to develop a robust needle detection and tracking method for the liver biopsy guidance. The current work consists in a simulation validation of the robustness of the proposed technique. The study will now be extended to ex-vivo and in vivo tests. In real 3D US volume, some more challenges like electronic noise, the difficulty to separate the needle tip, and the physiological motion can appear.

Electronic noise is usually considered as additive white Gaussian noise in ultrasonic imaging. With the increase of the depth, the influence of electronic noise will be larger because of the attenuation of the US signal. The main effect of this kind of noise in our method will be in the speckle tracking step. As the NCC is calculated, the electronic noise will lead to a miss match between the kernel region and the right target in the searching region. A step of noise compression could be added to limit the effect of the electronic noise.

The second challenge is the precise tracking of the needle tip. Because of its small size, the needle tip reflects less US wave, which can cause a shadow at the tip compared with the whole

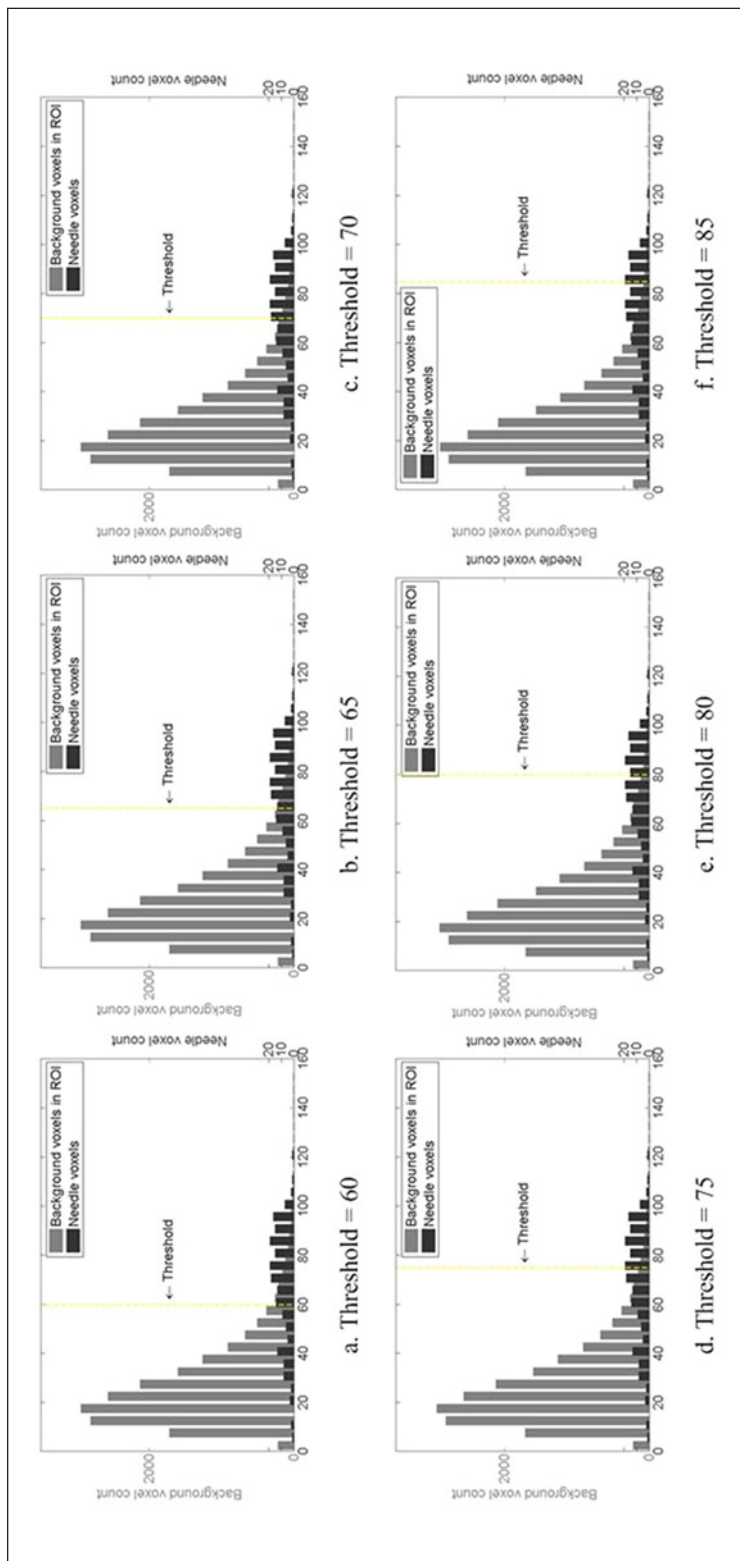


Figure 6. The histogram of background voxels in the ROI and needle voxels.
 Note. The vertical dashed line represents the threshold value. The threshold value changes with $CR = 2.5$. Note that to be able to observe well the different counts of the background voxels and the needle voxels, the scales of the left and right y-axes are not the same. ROI = region of interest; CR = contrast ratio.

Table 4. The Average Inliers Count with Different Thresholds from 60 to 75, with CR = 2.5.

CR	2.5					
Threshold	60	65	70	75	80	85
Inliers count	223	200	179	153	123	85

Note. CR = contrast ratio.

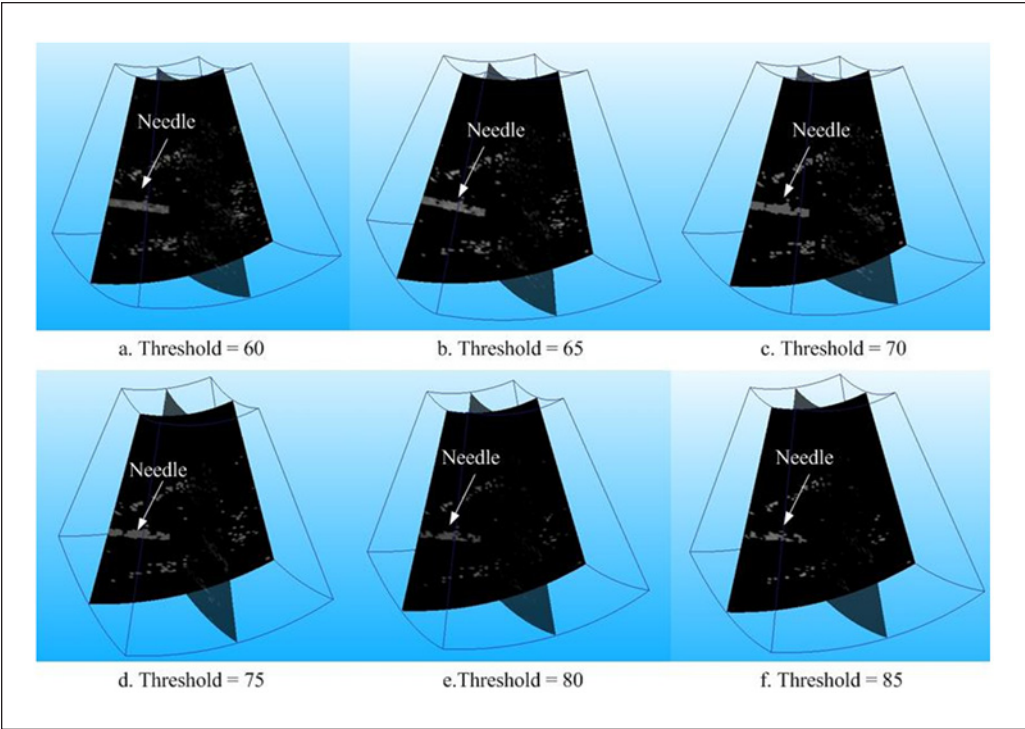


Figure 7. Different appearances of a needle in the 3D US volumes after the different thresholds, CR = 2.5. Note. 3D US = three-dimensional ultrasound; CR = contrast ratio.

image of the needle; however, because some tissue could shelter the US wave, certain parts of the needle could appear as dark as the surrounding tissue in the US image. In this situation, the tip could be considered as a hot pixel and ignored by the radiologist. What’s more, if the tip of the needle is not well located, the risk of injury for the human tissue or organ increases. As a result, precise tracking of the needle tip is very important in clinical applications.

The two challenges mentioned above are less problematic in ex-vivo experiments. However, in the clinical applications, the physiological motion of the liver cannot be negligible. The motion of the liver tissue is mainly caused by respiration. In Bell et al.,³² it is claimed that the mean peak-to-trough displacements of liver motion span is 5 to 40 mm in the superior–inferior direction under normal respiratory conditions. As our work has not yet reached the in vivo applicability, our model does not include the information of tissue motion. A tissue motion model will probably be implemented in the control vector and control matrix (Appendix C, Equation (C1)) of the Kalman filter to make the ROI-RK method closer to the real applications.

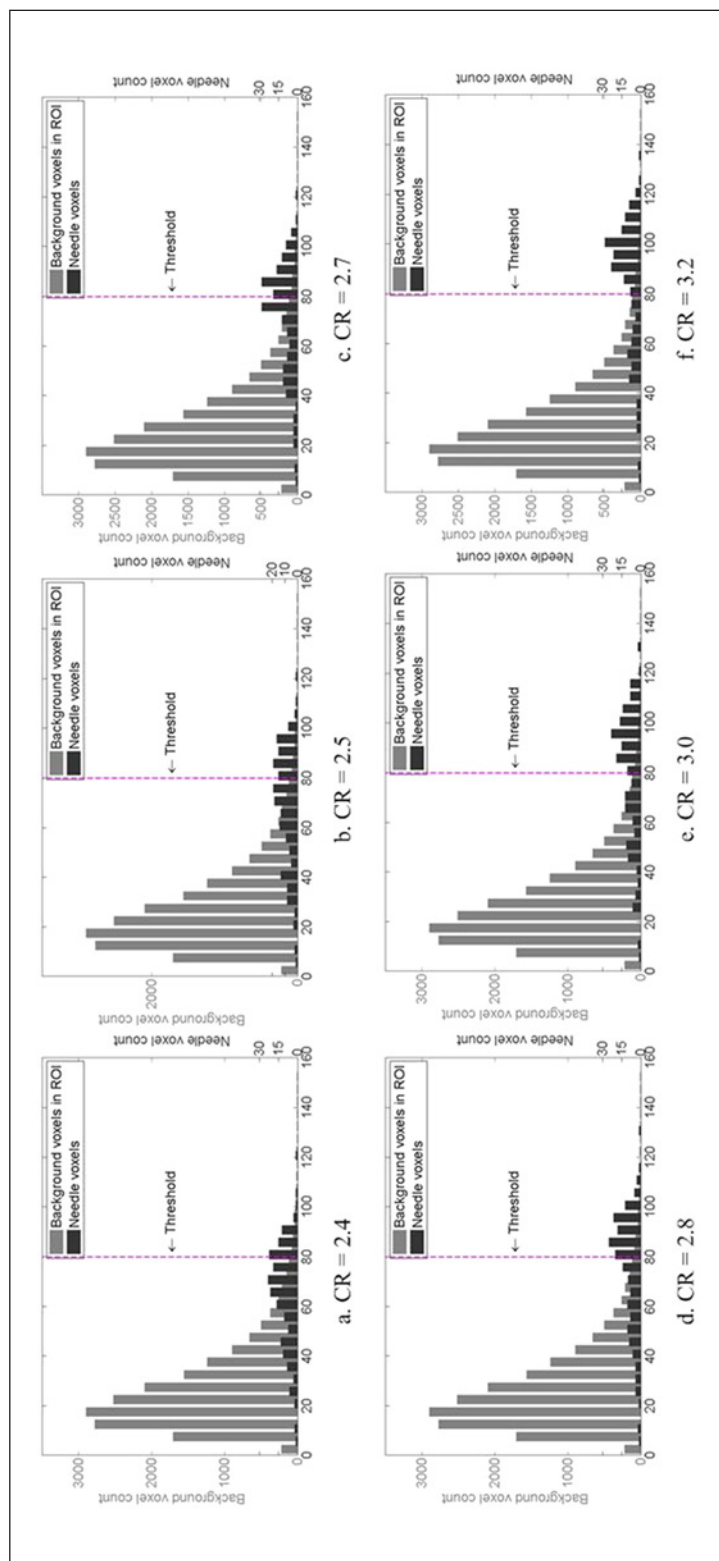


Figure 8. The histogram of background voxels in the ROI and needle voxels. Note. The vertical dashed line represents the threshold value. The CR is from 2.4 to 3.2, with the threshold = 85. Note that to be able to observe well the different counts of the background voxels and the needle voxels, the scales of the left and right y-axes are not the same. ROI = region of interest; CR = contrast ratio.

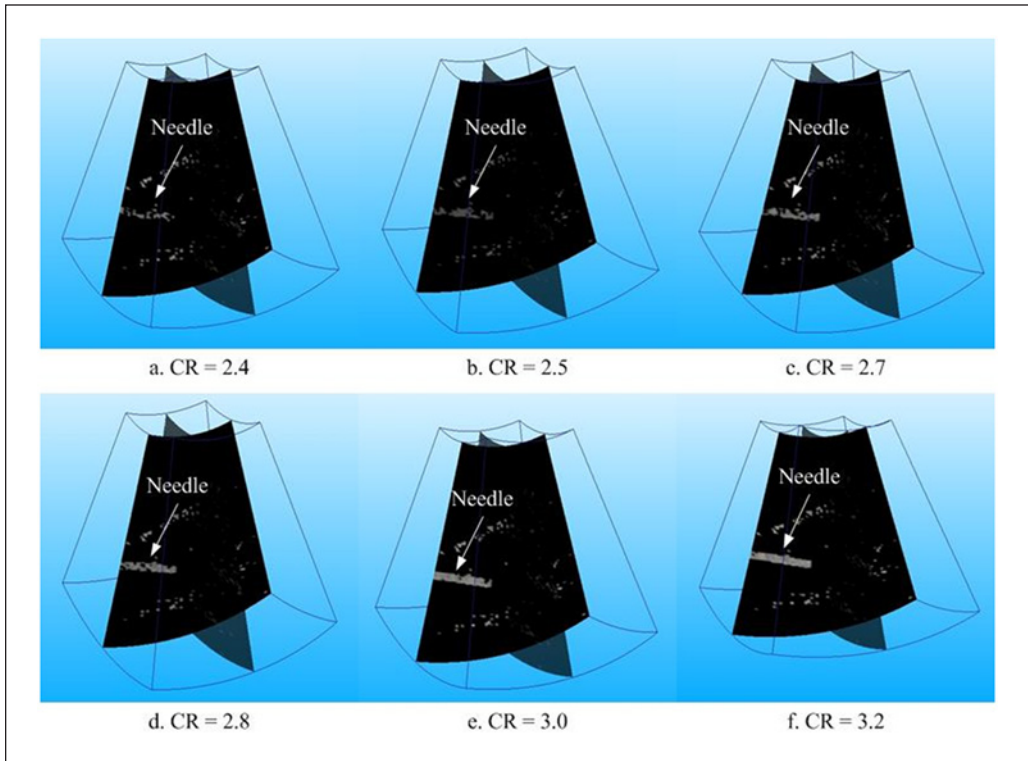


Figure 9. Different appearances of a needle in the 3D US volumes after the same threshold, with different CRs from 2.4 to 3.2.

Note. 3D US = three-dimensional ultrasound; CR = contrast ratio.

Conclusion

An ROI-RK method for tool localization and tracking from a 3D US volume is proposed in this article. This method uses the model-fitting RANSAC algorithm for tool localization and the Kalman filter and motion estimation method for tracking. To enhance the robustness and reduce the processing time, an automatic ROI-choosing strategy is included in the proposed ROI-RK method. Thanks to the line filter and RANSAC, the ROI can be initialized automatically as a cylinder region. The shape of the ROI further enhances the stability of needle localization and tracking, and the limitation of voxels increases the computational speed. The simulations proved that the proposed method has a better performance than the RANSAC algorithm. Moreover, it can meet the current requirements concerning processing time in clinical practice.

Future extensions include adding a self-correction feature in the ROI-RK method, because the proposed method will fail when the background gets too noisy. An auto-ROI-correction system is also under consideration in case of a great relative motion between the probe and the needle. In this case, the new position of the needle will be out of the ROI, and the update ROI procedure of the Kalman filter will be invalid. We are considering adding a parameter like the angle difference or axis difference in our existing system, and when this parameter passes some preset threshold value, a new ROI will be regenerated automatically. An executable software for clinical use is also under development.

Appendix A

Line Filter

In Frangi et al.,²⁴ the intensity variation of the voxel V is evaluated using the second-order derivatives. The Taylor expansion of an image function $I(M)$ at the point M_0 is

$$I(M_0 + \Delta M_0) = I(M_0) + \Delta M_0^T \nabla I(M_0) + \frac{1}{2} \Delta M_0^T H(M_0) \Delta M_0, \quad (A1)$$

where $H(M_0)$ is the Hessian matrix:

$$H(M_0) = \begin{bmatrix} I_{xx}(M_0) & I_{xy}(M_0) & I_{xz}(M_0) \\ I_{yx}(M_0) & I_{yy}(M_0) & I_{yz}(M_0) \\ I_{zx}(M_0) & I_{zy}(M_0) & I_{zz}(M_0) \end{bmatrix}. \quad (A2)$$

According to the concepts of the linear scale space theory,²⁴ the derivatives of the image $I(M)$ are defined as a convolution with the derivatives of Gaussian function:

$$I_x(M) = I(M) \times \frac{\partial}{\partial x} G(M, s), \quad (A3)$$

$$I_{xy}(M) = I(M) \times \frac{\partial}{\partial x \partial y} G(M, s). \quad (A4)$$

$G(M, S)$ is the three-dimensional (3D) Gaussian kernel defined as

$$G(M, s) = \frac{1}{\sqrt{2\pi s^2}^3} \exp\left(-\frac{\|M\|^2}{2s^2}\right). \quad (A5)$$

Here, s is the scale and it is also the expected radius of the needle.

The Hessian matrix contains the second-order information of the local structure. Suppose that λ_1, λ_2 , and λ_3 are the eigenvalues of the Hessian matrix, and $|\lambda_1| \leq |\lambda_2| \leq |\lambda_3|$. According to Frangi et al.,²⁴ for an ideal bright tubular structure with a dark background, the three eigenvalues satisfy

$$|\lambda_1| \ll |\lambda_2| \approx |\lambda_3| \text{ and } \lambda_1 \approx 0 \text{ and } \lambda_2 < 0, \lambda_3 < 0. \quad (A6)$$

Frangi et al. have proposed an advanced tubularness measure by introducing three natural quantities— R_B distinguishes the structure from a blob-like pattern:

$$R_B = \frac{|\lambda_1|}{\sqrt{|\lambda_2 \lambda_3|}}. \quad (A7)$$

R_A distinguishes between plate-like and line-like structures:

$$R_A = \frac{|\lambda_2|}{|\lambda_3|}, \quad (A8)$$

and S quantifies the needle voxels and background voxels:

$$S = \|H\|_F = \sqrt{\sum_{i=1}^3 \lambda_i^2}. \quad (A9)$$

Frangi et al. also define a tubularness measurement function:

$$T(M) = \left(1 - \exp\left(-\frac{R_A^2}{2\alpha^2}\right)\right) \exp\left(-\frac{R_B^2}{2\beta^2}\right) \left(1 - \exp\left(-\frac{S^2}{2c^2}\right)\right), \quad (A10)$$

where α , β , and c are parameters that control the sensitivity of $T(M)$ to measure R_B , R_A , and S . The recommended value of α and β is 0.5 and $c = 1/2 \arg\max(\lambda_i^2)$, $i = 1, 2, 3$. Thus, for the initialization of ROI, the tubularness of the ultrasound (US) image is measured instead of the image intensity.

Appendix B

Model-Fitting Random Sample Consensus (RANSAC)

Intensity classifying. Supposing that $V(M(x, y, z), I(M))$ represents the voxels of a three-dimensional ultrasound (3D US) volume, and there are two characteristics for each voxel: $M(x, y, z)$ represents the position and $I(M)$ represents the intensity of the voxel. The voxels are separated into two disjoint sets by classifying their intensities by a threshold: V_{th} is the voxels whose intensities are larger than threshold value and V_b is considered as the voxels of background:

$$\begin{aligned} V_{th} &= \{M \in V \mid I(M) \geq T_l\} \\ V_b &= V - V_{th}. \end{aligned} \quad (B1)$$

Here, T_l is the threshold value. It is chosen by the assumption that 99% of the voxels are from the background surrounding tissue. Even under this assumption, V_{th} also contains some non-needle voxels whose intensity is larger than T_l .

Axis shape model. The parametric equation for a 3D straight line is

$$l(t; \mathbf{A}) = \begin{bmatrix} a_{11} & a_{12} \\ a_{21} & a_{22} \\ a_{31} & a_{32} \end{bmatrix} \begin{bmatrix} 1 \\ t \end{bmatrix}, t \in \mathbb{R}, \quad (B2)$$

where $\mathbf{A} = \begin{bmatrix} a_{11} & a_{12} \\ a_{21} & a_{22} \\ a_{31} & a_{32} \end{bmatrix}$ is the coefficient matrix and t is the parameter.

From Equation (B12), it is obvious that the straight line can be determined by two control points N_1 and N_2 . The two parameters t_1 and t_2 are set as

$$\begin{aligned} t_1 &= 0 \\ t_2 &= \|N_1 - N_2\|. \end{aligned} \quad (B3)$$

Then, the matrix \mathbf{A} can be solved as follows:

$$\mathbf{A} = [N_1 \quad N_2] \begin{bmatrix} 1 & 1 \\ t_1 & t_2 \end{bmatrix}^{-1}. \quad (B4)$$

The axis shape model simply evaluates the distance from $M \in V_{th}$ to the line $l(t; \mathbf{A})$. A classifier function $q(N; \mathbf{A}) \in \{0, 1\}$ is defined as

$$q(N; \mathbf{A}) = \begin{cases} 1, & \text{if } d(N; \mathbf{A}) < r, \\ 0, & \text{otherwise} \end{cases}, \quad (B5)$$

where r is the expected radius of the needle in the image. All the voxels satisfying $q(N; \mathbf{A}) = 1$ are called the inliers V_{inl} , the other records are outliers. To evaluate the fitness of the inliers V_{inl} with respect to $l(t; \mathbf{A})$, a cost function is defined as

$$C(V_{inl}; \mathbf{A}) = \sum_{M \in V_{inl}} d(M; \mathbf{A}). \quad (B6)$$

Once $l(t; \mathbf{A})$ is chosen, $C(V_{inl}; \mathbf{A})$ is calculated. According to the value of cost function, the best-fitting model can be chosen. This best value is used in the step of optimization.

RANSAC algorithm. The RANSAC algorithm is used to estimate the optimal axis as the position of the needle. Given a sample set with a large number of outliers, the RANSAC uses the smallest possible set to form the model. In this case, the input data set is the thresholded voxels V_{th} and the classifier function $q(N; \mathbf{A})$. The output of RANSAC is the estimated axis and the data set \hat{V}_{inl} corresponds to this axis.

During each RANSAC iteration, n distinct points N_n are randomly selected from V_{th} to form the model. The model is a 3D space line, that is, $n = 2$. The set is defined as $N = \{N_i, i = 1, 2\}$. Samples with $\kappa(N) < d_{min}$ are rejected, where $\kappa(\bullet) = \|N_i - N_j\|, i \neq j$, and d_{min} is the smallest distance between the different points. After N is chosen, the coefficient matrix \mathbf{A} can be calculated by Equation (B4), and the set of inliers can also be obtained:

$$V_{inl}(\mathbf{A}) = \{N \in V_{th} \mid q(N; \mathbf{A}) = 1\}. \quad (B7)$$

The initial number of the iteration J is set to J_{max} (typically a few hundred, because it is time-consuming). However, the RANSAC algorithm has the capacity to update the iteration number adaptively. When a better model is found, the number of iteration is updated using^{16,33}:

$$J = \frac{\ln(1-\eta)}{\ln(1-\zeta^n)} \text{ with } \zeta = \frac{|V_{inl}|}{|V_{th}|}, \quad (B8)$$

where ζ is the inliers ratio and η is a parameter predefined by user, which indicates a desired probability that RANSAC succeeds; $P = \zeta^n$ is the probability that n randomly selected points are all from the V_{inl} .

Local optimization and tip localization. As the RANSAC procedure only gives an approximation of the axis position, the local optimization is used to get a more accurate result. The local optimization procedure is only done with the estimated set of inliers \hat{V}_{inl} .¹⁷ The more accurate axis position is found by minimizing the cost function (Equation B6).

Once the optimal axis has been found, the tip estimating process begins. According to Assumption (1) (section 0), on the needle axis, the voxel intensities drop sharply at the end of the needle. The needle is inserted from the outside, and thus only one tip needs to be located in the image. All the intensities of the voxels along the optimal axis are calculated, and a significant drop below the threshold value is considered as the tip position, shown in Figure B1.

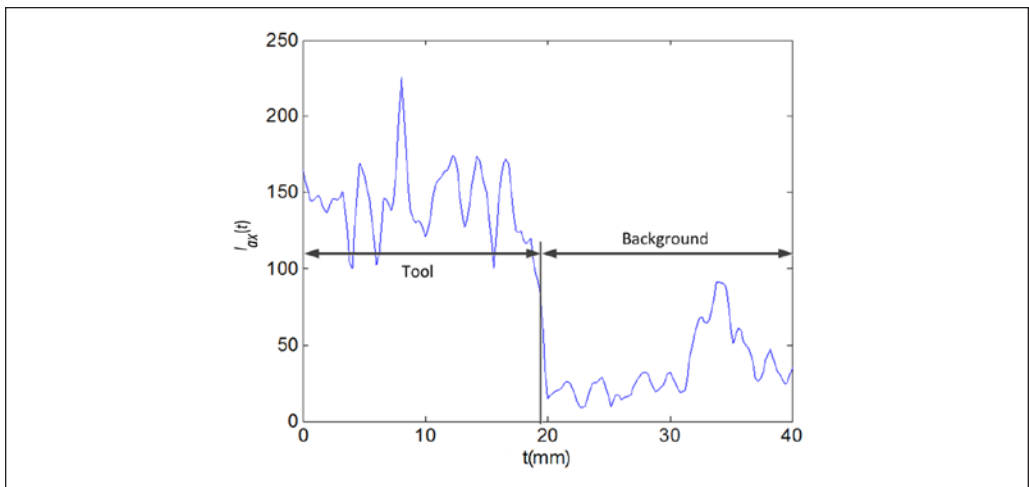


Figure B1. Illustration of the intensity curve along the needle axis.

Appendix C

Kalman Filter

The Kalman filter is an optimal recursive data-processing algorithm. It was first published in 1960 by Kalman.²⁵ The Kalman filter is a set of mathematical equations that provide an efficient computational means of estimating the state of a process, in a way that minimizes the mean of the squared error.³⁴ This filter is powerful to estimate the past, present, and even the future state of a system, and thus it is very useful for the prediction of needle position.

The k th state vector $\mathbf{s}_k \in \mathcal{R}^n$ is governed by the linear difference equation:

$$\mathbf{s}_k = \mathbf{F}\mathbf{s}_{k-1} + \mathbf{B}\mathbf{u}_{k-1} + \mathbf{w}_{k-1}. \quad (\text{C1})$$

With a measurement $\mathbf{z}_k \in \mathcal{R}^m$,

$$\mathbf{z}_k = \mathbf{H}\mathbf{x}_k + \mathbf{v}_k. \quad (\text{C2})$$

Here, $\mathbf{F}(n \times n)$ is the state transition matrix; \mathbf{B} is the control matrix; $\mathbf{H}(m \times n)$ expresses the relationship between the measurement vector and the state vector; \mathbf{u}_k is the input control vector; and \mathbf{w}_k and \mathbf{v}_k represent the process noise and measurement noise, respectively.

The five main equations in the Kalman filter can be divided into the following two parts:

The time updates equations:

$$\hat{\mathbf{s}}_k^- = \mathbf{F}\hat{\mathbf{s}}_{k-1} + \mathbf{B}\mathbf{u}_{k-1}, \quad (\text{C3})$$

$$\mathbf{P}_k^- = \mathbf{F}\mathbf{P}_{k-1}\mathbf{F}^T + \mathbf{Q}, \quad (\text{C4})$$

and the measurement updates equations:

$$\mathbf{K}_k = \mathbf{P}_k^- \mathbf{H}^T (\mathbf{H}\mathbf{P}_k^- \mathbf{H}^T + \mathbf{R})^{-1}, \quad (\text{C5})$$

$$\hat{\mathbf{s}}_k = \hat{\mathbf{s}}_k^- + \mathbf{K}_k (\mathbf{z}_k - \mathbf{H}\hat{\mathbf{s}}_k^-), \quad (\text{C6})$$

$$\mathbf{P}_k = (\mathbf{I} - \mathbf{K}_k \mathbf{H}) \mathbf{P}_k^-. \quad (\text{C7})$$

Here, $\hat{\mathbf{s}}_k^-$ represents the a priori estimated state, and $\hat{\mathbf{s}}_k$ is the a posteriori estimated state in step k ; \mathbf{P}_k^- is the a priori estimated error covariance, and \mathbf{P}_k is the a posteriori estimated covariance at step k . \mathbf{R} and \mathbf{Q} are the measurement error covariance and processing error covariance, respectively. \mathbf{K}_k is the Kalman gain.

Acknowledgment

This work was performed within the framework of the LABEX CELYA (ANR-10-LABX-0060) and LABEX PRIMES (ANR-11-LABX-0063) of Université de Lyon, within the program “Investissements d’Avenir” (ANR-11-IDEX-0007) operated by the French National Research Agency (ANR).

Declaration of Conflicting Interests

The author(s) declared no potential conflicts of interest with respect to the research, authorship, and/or publication of this article.

Funding

The author(s) received no financial support for the research, authorship, and/or publication of this article.

References

1. Krupa A, de Mathelin M, Doignon C, Gangloff J, Morel G, Soler L, et al. Automatic 3-d positioning of surgical instruments during robotized laparoscopic surgery using automatic visual feedback. In: Dohi T, Kikinis R, ed. *Medical Image Computing and Computer-Assisted Intervention—MICCAI 2002*. Berlin, Germany: Springer; 2002. pp. 9-16.
2. Bax J, Cool D, Gardi L, Knight K, Smith D, Montreuil J, et al. Mechanically assisted 3D ultrasound guided prostate biopsy system. *Med Phys*. 2008;35(12):5397-410.
3. Hong J, Dohi T, Hashizume M, Konishi K, Hata N. An ultrasound-driven needle-insertion robot for percutaneous cholecystostomy. *Phys Med Biol*. 2004;49(3):441-55.
4. Allen DW, Brady PS, Matalon TAS. Ultrasound guidance in interventional radiology. *Contemp Diagn Radiol*. 2006;29(3):2-7.
5. Chin KJ. Ultrasound guided needle insertion and injection skills. In: 9th Annual International Symposium of Ultrasound for Regional Anesthesia and Pain Medicine, Toronto, Ontario, Canada, 22-25 June 2012, pp. 1-8.
6. Fronheiser MP, Idriss SF, Wolf PD, Smith SW. Vibrating interventional device detection using real-time 3-D color Doppler. *IEEE Trans Ultrason Ferroelectr Freq Control*. 2008;55(6):1355-62.
7. Nichols K, Wright LB, Spencer T, Culp WC. Changes in ultrasonographic echogenicity and visibility of needles with changes in angles of insonation. *J Vasc Interv Radiol*. 2003;14(12):1553-7.
8. Rotemberg V, Palmeri M, Rosenzweig S, Grant S, Macleod D, Nightingale K. Acoustic radiation force impulse (ARFI) imaging-based needle visualization. *Ultrason Imaging*. 2011;33(1):1-16.
9. Draper K, Blake C, Gowman L, Downey D, Fenster A. An algorithm for automatic needle localization in ultrasound-guided breast biopsies. *Med Phys*. 2000;27(8):1971-9.
10. Wei Z, Gardi L, Downey DB, Fenster A. Oblique needle segmentation for 3D TRUS-guided robot-aided transperineal prostate brachytherapy. In: *IEEE International Symposium on Biomedical Imaging: Nano to Macro*, 15-18 April 2004, pp. 960-3.
11. Wei Z, Ding M, Downey D, Fenster A. 3D TRUS guided robot assisted prostate brachytherapy. *Med Image Comput Comput Assist Interv*. 2005;3750:17-24.
12. Hartmann P, Baumhauer M, Rassweiler J, Meinzer H-P. Automatic needle segmentation in 3D ultrasound data using a Hough transform approach. *Bildverarbeitung Für Die Medizin 2009*. 2009;37(2):341-5.
13. Zhou H, Qiu W, Ding M, Zhang S. Automatic needle segmentation in 3D ultrasound images using 3D improved Hough transform. *Proc SPIE Med Imag Parallel Process Images, Optim Techn (MIPPR)*. 2008;691821-691821-9.
14. Qiu W, Ding M, Yuchi M. Needle segmentation using 3D quick randomized Hough transform. In: 2008 First International Conference on Intelligent Networks and Intelligent Systems, 1-2 November 2008; Wuhan, China. pp. 449-52.
15. Barva M, Uhercik M, Mari J, Kybic J. Parallel integral projection transform for straight electrode localization in 3-D ultrasound images. *IEEE Trans Ultrason Ferroelectr Freq Control*. 2008;55(7):1559-69.
16. Fischler MA, Bolles RC. Random sample consensus: a paradigm for model fitting with applications to image analysis and automated cartography. *Commun ACM*. 1981;24(6):381-95.
17. Uherčík M, Kybic J, Liebgott H, Cachard C. Model fitting using RANSAC for surgical tool localization in 3-D ultrasound images. *IEEE Trans Biomed Eng*. 2010;57(8):1907-16.
18. Uherčík M, Liebgott H, Kybic J, Cachard C. Needle localization methods in 3D ultrasound data. In: *International Congress on Ultrasonics*, 11-17 January 2009; Santiago, Chile. pp. 17-20.
19. Uherčík M, Jan K, Christian C, Liebgott H. Line filtering for detection of microtools in 3D ultrasound data. In: *IEEE International Ultrasonics Symposium*, Rome, Italy, 20-23 September 2009, pp. 594-7.
20. Zhao S, Qiu W, Ming Y, Ding M. Needle segmentation in 3D ultrasound images based on phase grouping. In: *6th International Symposium on Multispectral Image Processing and Pattern Recognition*. 2009;74971L-74971L-10.

21. Jensen J. Field: a program for simulating ultrasound systems. *Med Biol Eng Comput.* 1996;34(Suppl. 1, pt. 1):351-3.
22. Jensen J, Svendsen NB. Calculation of pressure fields from arbitrarily shaped, apodized, and excited ultrasound transducers. *IEEE Trans Ultrason Ferroelectr Freq Control.* 1992;39(2):262-7.
23. Zhao Y, Liebgott H, Cachard C. Tracking micro tool in a dynamic 3D ultrasound situation using Kalman filter and RANSAC algorithm. In: 9th IEEE International Symposium on Biomedical Imaging (ISBI), Barcelona, Spain, 2-5 May 2012, pp. 1076-9.
24. Frangi AF, Niessen WJ, Vincken KL, Viergever MA. Multiscale vessel enhancement filtering. *Med Image Comput Comput Assist Interv.* 1998;1496:130-7.
25. Kalman RE. A new approach to linear filtering and prediction problems. *Trans ASME J Basic Eng.* 1960;82(Series D):35-45.
26. Building E. Speckle tracking for multi-dimensional flow estimation. *Ultrasonics.* 2000;38:369-75.
27. Robinson DE, Chen F, Wilson LS. Measurement of velocity of propagation from ultrasonic pulse-echo data. *Ultrasound Med Biol.* 1982;8(4):413-20.
28. Trahey GE, Allison JW, Von Ramm OT. Angle independent ultrasonic detection of blood flow. *IEEE Trans Biomed Eng.* 1987;34(12):965-7.
29. Lewis JP. Fast normalized cross-correlation. In: *Vision Interface. Canadian Image Processing and Pattern Recognition Society*, 1995, pp. 120-3.
30. Crow F. Summed area tables for texture mapping. *Comput Graph SIGGRAPH Proc.* 1984;18(3):200-20.
31. Duboeuf F, Basarab A, Liebgott H, Brusseau E, Delachartre P, Vray D. Investigation of PVA cryogel Young's modulus stability with time, controlled by a simple reliable technique. *Med Phys.* 2009;36:656-61.
32. Bell MA, Byram BC, Harris EJ, Evans PM, Bamber JC. In vivo liver tracking with a high volume rate 4D ultrasound scanner and a 2D matrix array probe. *Phys Med Biol.* 2012;57(5):1359-74.
33. Torr PH, Zisserman A, Maybank S. Robust detection of degenerate configurations while estimating the fundamental matrix. *Comput Vis Image Underst.* 1998;71(3):312-33.
34. Welch G, Bishop G. *An Introduction to the Kalman Filter (TR 95-041).* Chapel Hill: University of North Carolina at Chapel Hill; 2006.